Meteorologische Zeitschrift, Vol. 27, No. 2, 161–179 (published online January 31, 2018)

Classifying ground-measured 1 minute temporal variability within hourly intervals for direct normal irradiances

Marion Schroedter-Homscheidt[1*], Miriam Kosmale[1], Sandra Jung[2] and Jan Kleissl[3]

[1]Deutsches Zentrum für Luft- und Raumfahrt (DLR) e. V., Deutsches Fernerkundungsdatenzentrum (DFD), Oberpfaffenhofen, 82234 Wessling, Germany
[2]Former affiliation: DLR, Oberpfaffenhofen, Germany
[3]Center for Renewable Resources and Integration, Center for Energy Research, University of California, San Diego

(Manuscript received September 20, 2017; in revised form January 4, 2018; accepted January 5, 2018)

Abstract

Variability of solar surface irradiances in the 1 minute range is of interest especially for solar energy applications. Eight variability classes are defined for the 1 minute resolved direct normal irradiance (DNI) variability inside an hour. They combine high, medium, and low irradiance conditions with small, medium, and large scale variations from one minute to the next minute.

A reference data base of 333 individual hours with ground-based 1 minute DNI observations was created by expert review from one year of observations at the BSRN station in Carpentras, France. Each variability class is represented by 16 to 63 members.

Variability indices as previously published or newly suggested are used as classifiers to detect the class members automatically. Up to 77 % of all class members are identified correctly by this automatic scheme. The variability classification method allows the comparison of different project sites in a statistical and automatic manner to quantify short-term variability impacts on solar power production.

Keywords: variability, global horizontal irradiance, direct irradiance, automatic classification, ground-based observations

1 Introduction

Time series of surface solar irradiance are characterized by high variability on various scales. Obviously, there are seasonal cycles and daily extraterrestrial cycles due to sun geometry. These are well known and can be described in a deterministic manner based on astronomical laws (e.g. Iqbal, 1983). The variability of cloud free (also called clear sky) irradiances at the earth's surface is described in clear sky models as e.g. the Copernicus Atmosphere Monitoring Service (CAMS) McClear model (Lefévre et al., 2013).

Additional variability is introduced by atmospheric extinction caused mainly by aerosols, water vapour, and other atmospheric trace gases. The typical scale of aerosol optical depth variability was recently quantified by Schepanski et al. (2015). The total water vapor column varies on time scales as short as small eddies in the boundary layer to as long as global circulations. In general, the variability of irradiances caused by aerosols or water vapor – and by extension clear skies in general – is small on time scales of minutes.

Strong intra-hour variability results from extinction in clouds. Skartveit and Olseth (1992) found a bimodal pattern of one minute global horizontal irradiances (GHI) at various stations in Europe and the US which represents the typical changes between cloudy and cloud free conditions. Tovar et al. (2001) describe the one minute global irradiance distributions at Granada, Spain as an analytical single mode function around the hourly average GHI, but with different parameters for each class of clearness index (defined as ratio of GHI and top-of-atmosphere GHI) which also is an indicator for variable cloud conditions.

Ramping in irradiances may even occur on timescales as short as seconds (Tomson, 2010, Perez et al., 2011; Lave et al., 2012). For global irradiances, overshooting compared to clear sky irradiances or even to extra-terrestrial irradiances is observed as a result of three-dimensional scattering in clouds (Schade et al., 2007). Zehner et al. (2011) discuss that overshootings cause photovoltaic power (PV) to be up to 30 % larger than in cloud free conditions.

Such fast fluctuations of surface solar irradiances are of special concern in the solar energy sector. Suehrcke and McCormick (1989) and Vijayakumar et al. (2005) discuss the differences in using minutely and hourly GHI time series in 'usability assessments'. Jurado et al. (1995) investigate the statistical distribution of clearness index in five minute intervals and compare to hourly observations. Variability in GHI also causes strong ramps in PV based electricity generation and creates challenges

*Corresponding author: Marion Schroedter-Homscheidt, Deutsches Zentrum für Luft- und Raumfahrt e. V. (DLR), German Aerospace Center German Remote Sensing Data Center Oberpfaffenhofen, 82234 Wessling, Germany, e-mail: marion.schroedter-homscheidt@dlr.de

for the PV integration into the electrical grid (e.g. discussed in Wiemken et al., 2001; Lave and Kleissl, 2010; Jamaly et al., 2013; Lave et al., 2015). Perpignan et al. (2013) analyse time-dependent correlation between 5 sec resolved power measurements taken at inverters in a large scale photovoltaic power plant. Lohmann et al. (2016) investigate ramp rates and spatial correlation on the 1 sec scale as observed by 99 pyranometers within a 80 km^2 area. Remund et al. (2015) distinguish that the impact of second-to-second variability results in flicker effects, while the minute to hour variability influences regulation reserves and may create net load variability. Longer time scales of hours to days and months to years impact unit commitment and storage or capacity needs, respectively. The combination of photovoltaic systems with electrical storage can smooth PV generation, but may prevent battery capacity from being utilized for other purposes (e.g. peak shaving) or reduce the energy storage lifetime.

Hoff and Perez (2012) investigate the variability of a fleet of irradiance sensors distributed over an area of 400 m × 400 m and report a significant smoothing effect (defined here as correlation coefficients of ramp rates less than $1/e = 0.37$) for ratios of site pair distance to time scale of 7 m/s. For example, sites that are 100 m apart are uncorrelated over time scales less than 14 seconds. Hoff and Perez (2010) postulated and Kato et al. (2011), Perez et al. (2011), and Lave et al. (2013) confirmed that cloud speed affects spatio-temporal variability. For a review on spatio-temporal variability of solar irradiance see Perez et al. (2016). In specific in Fig. 6 of Perez et al. (2016) for a cloud speed of 20 km/h and 1 min data, station pairs became uncorrelated over distances of 150 m to 700 m depending on the correlation function. Based on these correlation functions and 700 hPa wind speeds to represent cloud speeds, Remund et al. (2015) suggest modeling time-space correlations of distributed PV production without measurements anywhere in the world. Aukai et al. (2016) report that averaging of GHI sensors distributed over less than 1 km leads to significant reduction of ramp rates on time scales below 1 min, but does not reduce ramp rates over 10 min to 60 min. 1 km is a typical spatial scale for a distribution grid and therefore these results motivate our focus on the variability on time scales larger than 1 min as even for high PV penetration such variability will not fully average out in a distribution grid. This is further supported e.g. by Anvari et al. (2016) who discuss the non-Gaussian properties of variability in wind and solar energy generation on the second and minute scale and how these properties exist even for a large number of power generators.

For concentrating solar thermal (CST) power, studies on 1 minute variabilty are lacking. Direct normal irradiance (DNI) variability is dampened in electricity generation through large thermal storage, which first store heat and later allow electricity generation on demand. Nevertheless, also CST power plants are affected by variability of the DNI in their solar field operations. For trough technologies the thermal inertia of the heat transfer fluid makes variability on the order of seconds or even one-minute of lesser concern. However, variability on the 10 min scale causes transient effects (Hirsch et al., 2015). On the other hand, in solar power tower technologies the variability on the minute scale is relevant as the thermal receiver may be damaged by fast and large temperature gradients. To avoid such gradients, the heliostats are frequently defocused and such a control system requires information on variability on and below the 1 minute scale (Hirsch et al., 2015).

A number of indices for the quantification of GHI variability on time scales of seconds, minutes, and hours have been suggested (Skartveit et al., 1998; Perez et al., 2011; Stein et al., 2012; Coimbra et al., 2013), while only Kraas et al. (2013) and Fernández-Peruchena et al. (2015) concentrate on metrics to describe DNI variability. Each of these variability indices was developed for GHI timeseries and for a specific application. They are sensitive to different aspects of variability in a time series such as magnitude or number of ramps or the frequency distributions of irradiance values. Here, they are adapted to DNI observations and used to classify variability automatically.

Section 2 presents the irradiance measurements. Section 3 reviews the literature on variability indices. Existing and new indices are used to quantify temporal irradiance variability comprehensively. Section 4 describes eight variability classes based on sub-hourly variability of 1 min resolved DNI time series. A reference database for variability index analysis is also presented. Section 5 provides the description of an automatic classification scheme for each hour of the time series, while Section 6 concludes the paper and provides an outlook on applications for such a classification.

2 Data

In this study only ground-based observations providing the direct and the global component are of interest. Direct irradiance measurements are highly sensitive to daily cleaning of the sensors and require a rigorous data quality control. Therefore, measurements from the Baseline Surface Radiation Network (BSRN, Ohmura et al., 1998) are used. BSRN stations provide ground-based datasets of GHI, DNI, and the diffuse sky irradiance component at 1 min temporal resolution. The quality control procedures are described in Long and Dutton (2012).

For the reference database and analysis in this paper the BSRN station in Carpentras (France) is selected. Carpentras is a Southern location with strong relevance for the solar energy sector and higher direct irradiance values compared to stations situated in Central and Northern Europe. It is a location with both Mediterranean and Central European climate resulting in various cloud types and therefore a wide range of irradiance variability conditions. Based on Meteosat Second

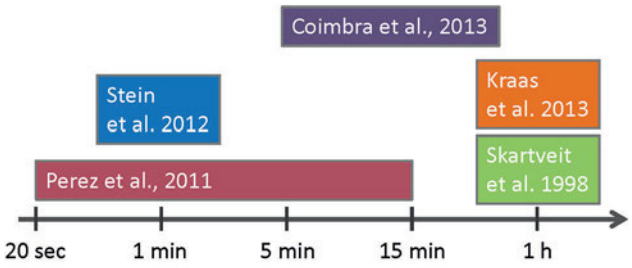

Figure 1: Temporal variability scales as investigated in existing studies.

Generation (MSG) cloud physical retrieval results, a statistical analysis of cloud occurrence for 2008 to 2013 following the method of Wey and Schroedter-Homscheidt (2014) reveals that 44 % of all daytime satellite-based observations are cloudy. Water and mixed phase clouds in low, medium, and high altitudes occur in 9, 11, and 7 % and high, thin ice clouds are found in 17 % of all daytime satellite observations. Low, medium, and high levels are separated by pressure levels of 700 and 400 hPa. Cloud occurrence is nearly equally distributed over the months of the year and the time of the day. Scattered cloud cases occur slightly more often than overcast conditions. The year 2012 is chosen for this study. Cloud statistics of 2012 are representative for the 2008 to 2013 period: Water and mixed phase clouds in low, medium, and high altitudes occur in 10, 9, and 7 % and high, thin ice clouds are found in 16 % of all daytime satellite observations.

In Section 5.4 the variability classification method is applied to BSRN data from other stations and compared to satellite-based statistics. The stations of Cabauw (The Netherlands), Sarriguren (Spain), and Izana (IZA, Spain) are chosen as they are located in different climates, provide observations for 2012, and are within the Meteosat Second Generation satellite field of view.

3 Variability indices

Several GHI variability indices have been published, but they have been applied to different time scales in the original studies (Fig. 1).

Skartveit et al. (1998) introduced a variability index σ_{Sk} based on the clear sky index of the actual hour t versus the previous $(t-1)$ and the following hour $(t+1)$. The differences are squared, averaged and a square root is taken (Eq. (3.1)). The clear sky index k_c is defined as the ratio between actually measured GHI and theoretically expected GHI in the cloud free case taken only Rayleigh scattering, trace gas absorption, and aerosol extinction into account.

$$\sigma_{\mathrm{Sk}} = \sqrt{\frac{(k_c(t)-k_c(t-1))^2+(k_c(t)-k_c(t+1))^2}{2}} \tag{3.1}$$

This index was applied to hourly pyranometer daytime observations at Bergen, Norway for the snow-free months April to October from 1965 to 1996. The index is dimensionless, has very small values in non-variable conditions and reaches typically 0.5 to 1.0 in broken cloud conditions. Here, this index is applied for 1 minute resolved GHI and DNI observations and using k_{cDNI} which is the equivalent to the clear sky index, but for the beam component. The beam clear sky index is calculated for three consecutive minutes. Overall, this results in 58 individual k_{cDNI} values within an hour, which are averaged to obtain a single value per hour.

Coimbra et al. (2013) define a variability index V as the standard deviation of temporal differences of k_c in a time interval Δt (Eq. (3.2)). Their application is solar forecast verification on various time scales.

$$V = \sqrt{\frac{1}{n}\sum_{t=1}^{n}(\Delta k_c)^2} \tag{3.2}$$

The index V is dimensionless. The more variable the irradiance, the larger the index value is. Here this equation is used for all 1 minute DNI measurements within an hour.

Stein et al. (2012) define a dimensionless variability index VI inside a time period as the ratio of the sum of n differences of sequential GHI values in W/m^2 versus the sum of n differences of sequential clear sky GHI (CSI) values over a given time period (Eq. (3.3)). The time step Δt in minutes between two consecutive GHI values is taken into account as well.

$$VI = \frac{\sum_{i=2}^{n}\sqrt{(GHI(i)-GHI(i-1))^2+\Delta t^2}}{\sum_{i=2}^{n}\sqrt{(CSI(i)-CSI(i-1))^2+\Delta t^2}} \tag{3.3}$$

In cloud-free, non-variable conditions the VI reaches values around 1, while overcast days with small GHI values are characterized by values close to zero. In more variable conditions the VI can reach values above 1. Calculating the sums in Eq. (3.2) for 1 min GHI observations during a day Stein et al. (2012) obtained daily variability indices up to 25. Here, the same formula is applied for 1 min measurements within an hour ($\Delta t = 1$ min, $n = 60$) to get an hourly VI.

All indices described so far make use of clear sky indices or the ratio of terms including all-sky and clear-sky radiation. They were developed independently from each other and applied for different temporal resolutions. To understand their correlation, Fig. 2 (GHI) and Fig. 3 (DNI) present density scatterplots for all available daytime hours in 2012 at Carpentras. Clear days with low variability (defined as $k_c > 0.82$ between 10 and 14 UTC) are excluded to avoid a large number of cases with small index values making the scatterplots unreadable. This temporal window is motivated by the approach described in Section 5.

A potential linear dependence is quantified using Spearman rank correlation coefficients. For GHI based indices of V vs. σ_{Sk} a rank correlation coefficient of 0.99

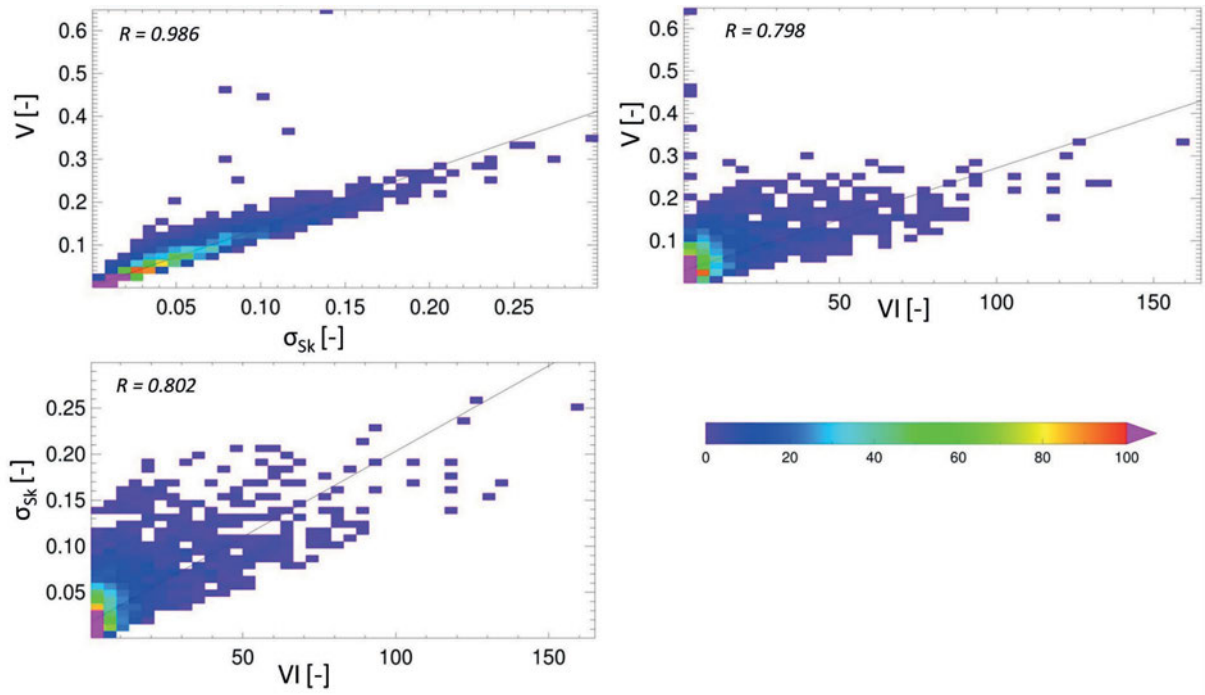

Figure 2: Density scatterplots of variability indices for GHI after Skartveit, Stein, and Coimbra et al. for the BSRN station Carpentras and 10 to 14 UTC hours on variable days in 2012 (Coimbra vs. Skartveit upper left, Coimbra vs. Stein upper right, and Skartveit vs. Stein lower left). The color bar indicates number of cases.

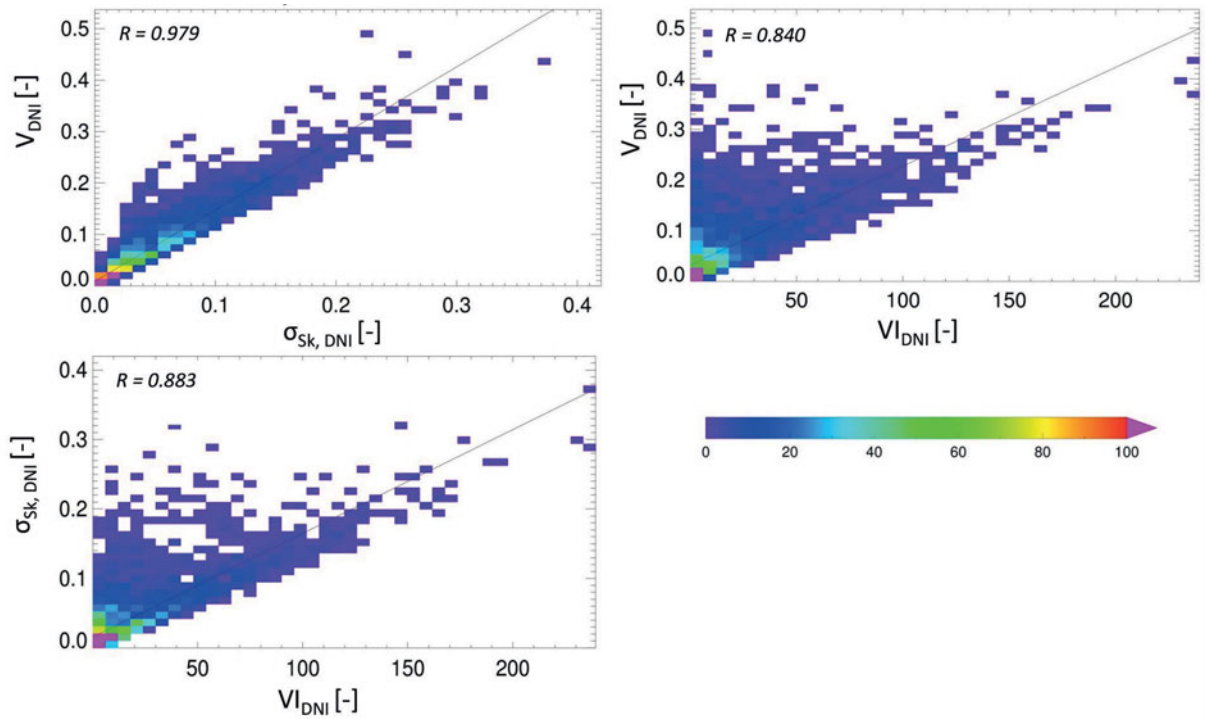

Figure 3: Density scatterplots of variability indices for DNI after Skartveit, Stein, and Coimbra et al. for the station BSRN Carpentras and 10 to 14 UTC hours on variable days in 2012 (Coimbra vs. Skartveit upper left, Coimbra vs. Stein upper right, and Skartveit vs. Stein lower left). The color bar indicates the number of cases.

is found, while σ_{Sk} vs. *VI* and *V* vs. *VI* result in rank correlation coefficients around 0.80. The same result is found for DNI. Overall, the DNI indices reach larger values as the DNI is more sensitive to clouds and can also reach zero values. DNI based indices of $\sigma_{Sk,DNI}$ vs. VI_{DNI} result in a rank correlation coefficient of 0.88, indices of V_{DNI} vs. VI_{DNI} result in 0.84, and indices of $\sigma_{Sk,DNI}$ vs. V_{DNI} result in 0.98. Therefore, for both GHI and DNI Skartveit and Coimbra's index are duplicative and Skartveit's index σ_{Sk} is excluded as the rank correlation between σ_{Sk} vs. *VI* is slightly higher than between *V* vs. *VI*.

Perez et al. (2011) describe variability inside an hour by the mean absolute Δk_{c_mean}, its standard deviation Δk_{c_σ} (which is similar to the *V* index) and the maximum absolute Δk_{c_max} of all differences in k_c within consecutive time instants. Time scales of 20 seconds, 1 min, 5 min, and 15 min are examined. Δk_{c_mean} is justified as the expected change of the irradiance between time steps. The standard deviation quantifies the width of the distribution of all irradiance changes. The maximum of all differences is a worst case estimate for the hour. In our study these indices are applied for the one minute resolved DNI observations within one hour as $\Delta DNI_{\_mean}$, the standard deviation $\Delta DNI_{\_\sigma}$ and the maximum $\Delta DNI_{\_max}$ and also for the k_{cDNI} values as mean Δk_{cDNI_mean}, the standard deviation Δk_{cDNI_σ} and the maximum Δk_{cDNI_max}.

Overshooting irradiances are defined as irradiances which reach higher values than the theoretical clear sky, defined here as a cloud-free atmosphere as provided by the CAMS McClear service (Lefévre et al., 2013). Overshootings are identified if the observed 1 minute GHI in a minute is enhanced more than 5 % or 10 % above the clear sky irradiance. The number of occurrences is counted and the indices are named OVER5 or OVER10, respectively.

Kraas et al. (2013) count the number of changes in the sign of the first derivative in DNI in a day on the basis of hourly DNI observations. The index is a predictor for the accuracy of day-ahead numerical weather prediction forecasts for electricity trading by assuming that variable days are related to lower forecast accuracy. Days with low variability typically have one change due to the noon maximum, while days with large variability show between 5 and 8 changes in the first derivative of hourly DNI.

Here, the same strategy is applied but for all local minima and maxima in the minute-by-minute observations within each hour. To avoid small variations to dominate the index, only extrema that differ from the next extremum by more than 15 % of the clear sky irradiance value are counted. This number is denoted CSFD (number of Changes in the Sign of the First Derivative). The same strategy is applied for GHI.

Finally, a new group of indices describing the upper and lower envelope of irradiance values is developed (Fig. 4). Please note that Fernández-Peruchena et al. (2015) independently suggested using an upper envelope to provide a dimensionless measure of the DNI variation, but their method defines the envelope curve differently and both methods should be clearly distinguished. While they define the upper envelope as the cloud-free DNI curve of a whole day, this study uses a different definition based on shorter time windows as in Jung (2015). First the time series is split into subsets of 4 min length and the local minima and maxima are identified. Second and in absence of extrema, the subset of the time series is extended by adding an adjacent 1 minute value until an extremum point (either a minimum or a maximum) is identified. These minima and maxima from different subintervals taken together constitute the upper and lower envelope time series. The first and last minute value of the original time series are added to ensure a continuous envelope time series. The approach may result in the identification of a local minimum in the vicinity of another local, but lower minimum in the neighboring 4 min window. Therefore, further quality control is performed: Adjacent minima within the hour are connected by a line. If there are values of the original time series below this line, they are added in the minimum envelope time series. An analogous procedure is applied to the maximum envelope. Note that for GHI the upper envelope can be above the clear sky value representing cloud overshootings due to three dimensional cloud effects.

The integral UML (integral of Upper Minus Lower) between the two envelopes is calculated for each hour. The difference between the upper and lower envelope is a measure of the intensity of short variation within a 4 min interval. For two cases with the same average k_{cDNI}, a larger UML integral value is caused by either more or deeper ramps occurring within the hour.

Another integral is calculated between the upper envelope and the clear sky time series (UMC, integral Upper Minus Clear). UMC quantifies how often and how much variations of DNI are away from the clear sky value. UMC is small (ideally zero) if the atmosphere is clear. Clouds cause the upper envelope to have smaller irradiance than the clear sky time series.

A third integral value for each hour is defined as the area between the lower envelope and the abscissa axis (LMA, integral Lower Minus Abscissa). LMA describes the aggregated depth of the variability occurring in an hour compared to the zero irradiance. The integral indices are applied for DNI only because unlike GHI it has no overshooting effects.

4 Variability classes

Harrouni et al. (2005), Koumparou et al. (2015) or Lorenz et al. (2016) classify individual days or multi-hour periods into variability classes, but in our work the daily or multi-hour classification was considered impractical as transitions between different cloud conditions result in different variability patterns during the

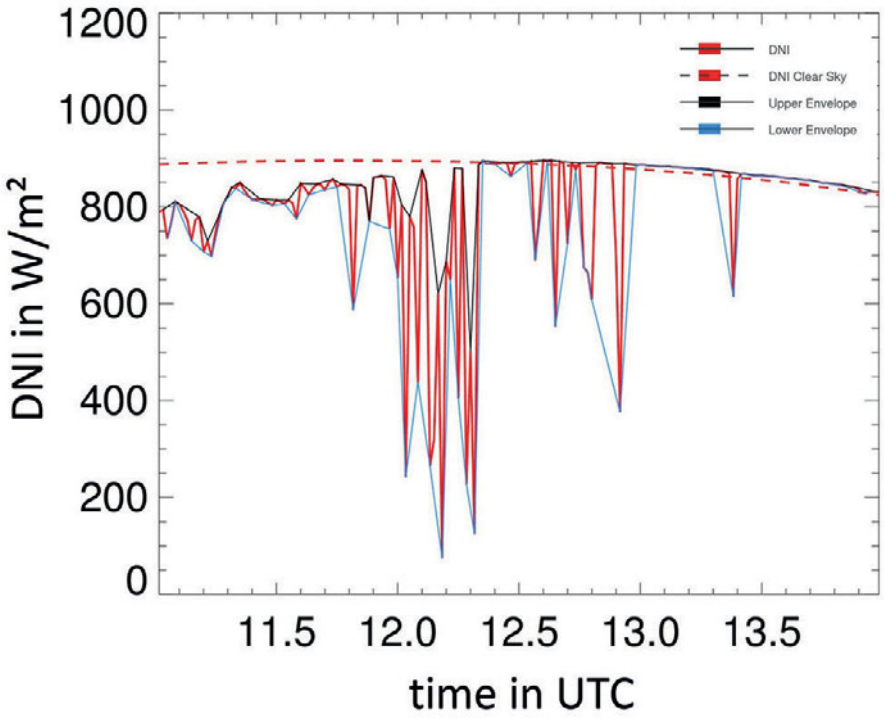

Figure 4: Example of upper and lower envelopes for an arbitrarily chosen day (22 January 2012) for BSRN Carpentras DNI observations.

day. Additionally, most existing power plant performance models use hourly resolved irradiance data as input. Therefore, this study aims at classifying the 1 min resolved variability within the hour by using generic variability classes.

As basis of the classification this study makes only use of DNI observations as DNI shows more intense variability compared to GHI where the diffuse component is always greater than zero. Using DNI allows a better separation of variability classes. Once the variability classes are defined, they are also described in their GHI variability characteristics in Section 4.3.

4.1 Manual classification

Eight classes are selected to characterize DNI variability. The selection is based on a visual interpretation of a year long time series by four different experts. Aside from shapes of the timeseries and knowledge of underlying meteorological phenomena, the classification was also influenced by expert knowledge on variability structures of importance to power plant operators, storage developers, solar project planners, and electricity grid operators. The selection is based on 1 min resolved DNI observations. Fig. 5 provides example hours (marked by red boxes) which are attributed to one of the eight classes by the experts.

Class 1 consists of cloud-free sky cases where the DNI follows the clear sky DNI. Class 2 consists of cases with nearly clear sky values and nearly no difference in the 10 min moving averages, but individual 1 min values vary from minute to minute. Class 3 also shows nearly clear sky values in the 10 min moving averages, but has a much stronger variability from minute to minute. Minute values may reach 30 to 50 % of the clear sky DNI which is already a strong reduction in few minutes within the hour. Class 4 shows large variability both from minute-to-minute and for consecutive 10 min moving averages. Individual minute DNI values may even approach zero. For Class 5, 10 min moving averages are significantly below the clear sky values; in this particular case a mean hourly k_{cDNI} of 0.75 is observed. Nevertheless, the additional variability from 1 minute to another minute is small to medium. Class 6 also has medium level DNI values like class 5, but the minute to minute ramps are very high. They may reach from zero to clear sky DNI values and provide the largest ramp magnitudes of all classes. Class 7 has very low average k_{cDNI}, but still some large ramps from minute to minute. Finally, class 8 consists of cases with zero or close to zero DNI and very small or no variability from minute to minute.

All hours with high sun elevation (between 9 and 14 UTC in 2012) at Carpentras were visually classified into the variability classes. Hours with perceived changes in variability class inside the hour were excluded. Such transition situations are frequent in real time series, but are not suited for the inclusion in the reference database. The database shall contain only those hours which can be attributed to a single variability class. Nevertheless, the natural variability within each class causes ambiguity and different visual classifications for certain hours. In other words, it is not always obvious to decide between neighbouring classes. This was accepted as it represents the continuum of natural

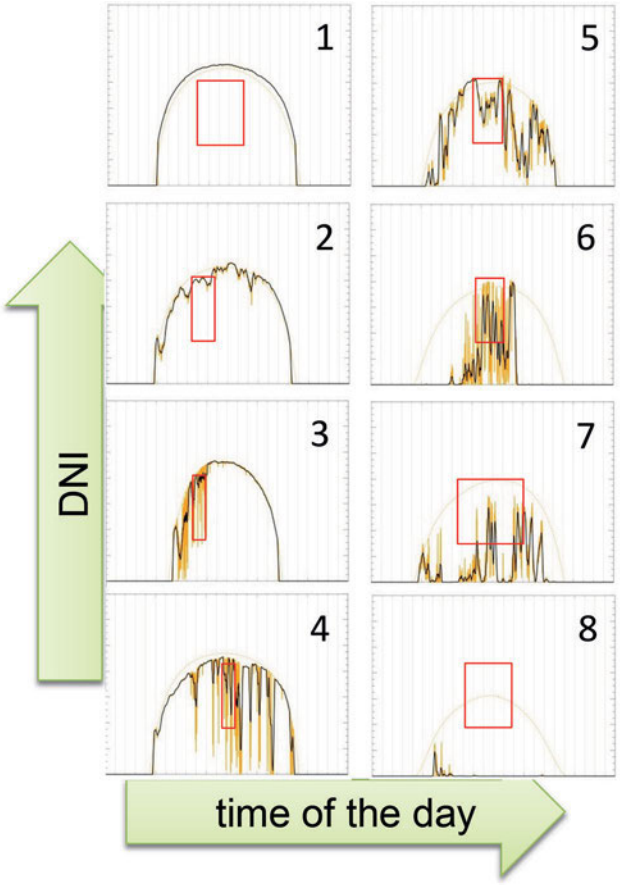

Figure 5: Arbitrarily chosen examples of the variability cloud classes 1 to 8 on 23 July, 11 May, 8 March, 15 July, 13 August, 5 July, 8 June, and 1 July 2012 (ordered as they appear with consecutive variability class names). Hours being classified in one of the classes are marked by a red box. Minute resolved DNI values (yellow), 10 min DNI moving averages (black) and clear sky DNI values (thin) are given.

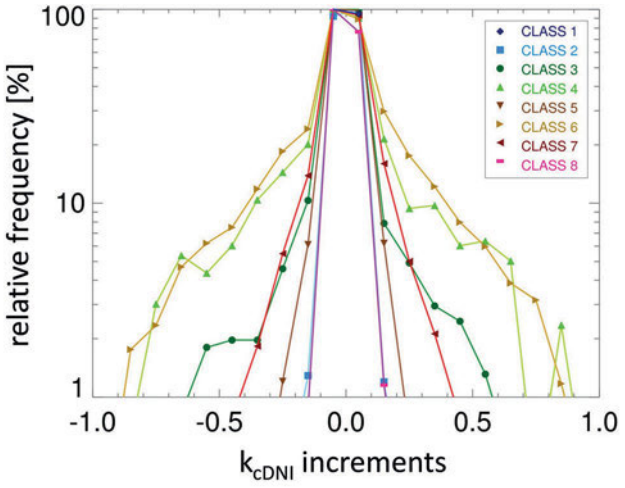

Figure 6: Relative frequency of minute-by-minute k_{cDNI} increment for all 8 variability classes.

variability and therefore makes the automatic classification developed later on more reliable.

This reference database of 333 cases is published with this paper and further described in Annex 1. The number of cases in each class ranges from 16 to 63 (Table 1).

4.2 DNI-based characterization

Overall, the classes are sorted from large to small k_{cDNI} (Table 1). As seen from Fig. 6 and Table 1 the 8 variability classes can be distinguished by median k_{cDNI}, CSFD, and the width of the distribution of k_{cDNI} increments.

Classes 1, 2, 5, and 8 have a small number of CSFD, classes 3 and 7 a medium number of CSFD and classes 4 and 6 have the largest numbers of CSFD.

Fig. 6 illustrates the typical minute-to-minute variability of all cases in the reference database. The frequency distributions of k_{cDNI} minute-by-minute increments differ remarkably between variability classes. Classes 4 and 6 show the highest minute-by-minute increments. Class 1 shows the lowest increments, which is difficult to observe in the figure as nearly all positive and negative increments are in the range [-0.1 0.1]. Similarly, the distributions of class 2 and class 8 have a small width. This is followed by class 5 and class 3. Class 3 has larger tails of large increments than classes 5 and 7 while it shows similar behaviour for smaller increments. Table 1 illustrates that even though the increment distribution is similar for some classes (as e.g. for classes 2 and 8 or 4 and 6) the median k_{cDNI} is systematically different.

Variability classes are also compared to each other via the previously published indices in Table 2 to 4. Classes 3, 4 and 6 show the same behaviour and are associated with the largest DNI based variability indexes.

4.3 GHI-specific characteristics

While the classes are defined with respect to DNI, the classes can also be described with respect to GHI. The variability indices are applied to the 1 minute resolved GHI observations and tabulated in Table 5 to 8. The number of direction changes in GHI, the number of overshootings above 5 % of the clear sky value (*OVER5*) and the number of overshootings above 10 % of the clear sky value (*OVER10*) are given in Table 5. For classes 2 to 8, the mean k_c is larger than the mean k_{cDNI} reflecting the diffuse contribution. The clear sky index for class 1 is slightly below 1.0 indicating that the CAMS McClear model slightly overestimates the Carpentras aerosol and/or trace gas columns. CSFD are slightly different for GHI compared to DNI, but the ranking remains the same. Class 6 shows the largest number of CSFD and the largest OVER5 and OVER10 counts. Class 6 is most variable, followed by classes 4, 7, and 3. The rankings are very similar to the DNI pattern, but the variability index magnitudes are of course different for the GHI observations.

Table 1: Variability class characterisation by k_{cDNI}, the number of direction changes in DNI within the hour, and the number of cases in the reference database. All median values and the P25 and P75 range (in brackets) are given.

class	short description	median k_{cDNI} [-]	CSFD in DNI [-]	#
1	very high DNI, low CSFD	0.99 (0.98, 1.04)	0 (0, 0)	63
2	high DNI, low CSFD	0.96 (0.93, 1.04)	0 (0, 2)	36
3	high DNI, medium CSFD	0.93 (0.91, 0.95)	8 (5, 12)	25
4	high DNI, medium CSFD	0.79 (0.75, 0.87)	16 (10, 17)	16
5	medium DNI, small CSFD	0.75 (0.68, 0.82)	3 (0, 6)	39
6	medium DNI, high CSFD	0.48 (0.35, 0.63)	15 (12, 19)	51
7	low DNI, medium CSFD	0.18 (0.12, 0.25)	7 (5, 9)	44
8	low DNI, low CSFD	0.00 (0.00, 0.01)	0 (0, 0)	38

Table 2: Variability class characterisation by ramp rates of clear sky indices with respect to DNI. All median values and the P25 and P75 range (in brackets) are given.

Class	Δk_{cDNI_mean} [-]	Δk_{cDNI_σ} [-]	Δk_{cDNI_max} [-]
1	0.00 (0.00, 0.00)	0.00 (0.00, 0.00)	0.01 (0.00, 0.01)
2	0.01 (0.01, 0.02)	0.02 (0.01, 0.02)	0.08 (0.06, 0.12)
3	0.06 (0.03, 0.09)	0.11 (0.06, 0.13)	0.45 (0.29, 0.58)
4	0.16 (0.12, 0.18)	0.21 (0.17, 0.24)	0.80 (0.68, 0.85)
5	0.03 (0.02, 0.05)	0.03 (0.02, 0.05)	0.13 (0.07, 0.20)
6	0.15 (0.12, 0.19)	0.18 (0.13, 0.23)	0.70 (0.58, 0.85)
7	0.06 (0.04, 0.08)	0.07 (0.05, 0.09)	0.30 (0.21, 0.41)
8	0.00 (0.00, 0.00)	0.00 (0.00, 0.01)	0.01 (0.00, 0.03)

Table 3: Variability class characterisation by ramp rates of DNI. All median values and the P25 and P75 range (in brackets) are given.

Class	$\Delta DNI_{\_mean}$ [W/m^2]	$\Delta DNI_{\_\sigma}$ [W/m^2]	$\Delta DNI_{\_max}$ [W/m^2]
1	1.2 (0.8, 1.4)	1 (0.8, 1.2)	4 (3, 5)
2	11.5 (5.6, 14.5)	13.3 (6.8, 21.8)	62 (36, 96)
3	51.9 (30.6, 82.6)	96.8 (49.6, 118.2)	414 (257, 483)
4	130.3 (108.0, 168.2)	187.2 (139.4, 216.1)	730 (542, 774)
5	23.3 (14.3, 40.0)	22.9 (12.8, 40.4)	109 (55, 185)
6	118.1 (91.2, 155.0)	143.4 (112.5, 173.8)	569 (477, 674)
7	49.3 (34.4, 58.7)	57.0 (37.4, 69.2)	238 (171, 323)
8	0.3 (0.1, 1.8)	0.8 (0.3, 4.2)	4 (1, 17)

Table 4: Variability class characterisation by variability indices after Stein et al. (2012), Coimbra et al. (2013) and the integral of upper minus lower envelopes for DNI. All median values and the P25 and P75 range (in brackets) are given.

Class	VI_{DNI} [-]	V_{DNI}[-]	UML [Wh/m^2]
1	1.47 (1.29, 1.74)	0.00 (0.00, 0.00)	1.46 (0.89, 1.93)
2	9.95 (5.63, 14.38)	0.02 (0.01, 0.03)	14.04 (6.95, 20.83)
3	42.28 (28.05, 65.61)	0.13 (0.07, 0.15)	74.40 (48.87, 123.01)
4	116.55 (98.45, 153.83)	0.26 (0.19, 0.30)	188.54 (152.64, 256.29)
5	22.96 (14.04, 34.72)	0.04 (0.02, 0.06)	33.95 (19.53, 58.40)
6	105.63 (83.73, 149.02)	0.23 (0.19, 0.29)	176.98 (132.65, 242.19)
7	41.27 (26.38, 51.17)	0.09 (0.06, 0.12)	67.81 (46.08, 86.69)
8	1.08 (0.96, 2.25)	0.00 (0.00, 0.01)	0.37 (0.13, 2.15)

Table 5: Variability class characterisation with respect to GHI – mean k_c, the number of CSFD in GHI, OVER5, and OVER10 per hour. All median values and the P25 and P75 range (in brackets) are given.

Class	mean k_c	CSFD in GHI	OVER5	OVER10
1	0.96 (0.95, 0.98)	0 (0, 0)	0 (0, 0)	0 (0, 0)
2	0.97 (0.95, 0.99)	0 (0, 1)	0 (0, 0)	0 (0, 0)
3	0.96 (0.93, 0.97)	6 (4, 9)	0 (0, 6)	0 (0, 0)
4	0.89 (0.87, 0.94)	14 (11, 17)	11 (2, 15)	0 (0, 9)
5	0.92 (0.86, 0.94)	2 (0, 5)	0 (0, 2)	0 (0, 0)
6	0.77 (0.70, 0.88)	14 (10, 18)	12 (6, 18)	7 (2, 13)
7	0.69 (0.58, 0.76)	7 (5, 9)	0 (0, 4)	0 (0, 1)
8	0.24 (0.15, 0.33)	0 (0, 2)	0 (0, 0)	0 (0, 0)

Table 6: Variability class characterisation by ramp rates of clear sky indices with respect to GHI (after Perez et al., 2011). All median values and the P25 and P75 range (in brackets) are given.

Class	$\Delta k_{c\_\mathrm{mean}}$	Δk_{c_σ}	$\Delta k_{c\_\mathrm{max}}$
1	0.00 (0.00, 0.00)	0.00 (0.00, 0.00)	0.00 (0.00, 0.01)
2	0.01 (0.01, 0.01)	0.01 (0.01, 0.02)	0.06 (0.04, 0.09)
3	0.05 (0.03, 0.07)	0.09 (0.05, 0.11)	0.37 (0.24, 0.44)
4	0.13 (0.11, 0.15)	0.19 (0.14, 0.21)	0.67 (0.52, 0.74)
5	0.02 (0.01, 0.04)	0.02 (0.01, 0.04)	0.11 (0.05, 0.18)
6	0.12 (0.10, 0.16)	0.15 (0.11, 0.17)	0.55 (0.48, 0.68)
7	0.06 (0.04, 0.07)	0.06 (0.04, 0.07)	0.25 (0.19, 0.34)
8	0.01 (0.00, 0.02)	0.01 (0.00, 0.02)	0.03 (0.01, 0.08)

5 Automatic classification

5.1 Correlation between variability indices

As a quality control step only hours with more than 50 valid 1 minute measurements are selected for the following analysis.

Based on the variability indices and the generic variability classes introduced in Section 4, the typical values of all indices and their distribution in each class are derived in the following.

For visualization purposes the indices are scaled to a range of −100 to 100 and the scaling factors are shown in Fig. 7. Fig. 7 is an example for variability class 3, similar plots for all classes can be found in Annex 2.

The visual interpretation of Fig. 7 for all classes (see Annex 2) indicates a grouping of some indices which behave similarly in each class, but (as a group) behave differently from one class to the other. These index groups are treated in the further classification as classifiers (see Section 5.3). Some classifiers consist only of a single index, others are composed of a group of indices.

In the following, the grouping of the variability indices is derived in a systematic approach. Indices within one group are compared against each other using Pearson correlation coefficients for the 2012 Carpentras data. Correlation heat maps for all classes are evaluated – individually for each class and aggregated over all classes. Fig. 8 shows the aggregated correlation statistic as a sum of the correlation coefficients for all 8 classes. If a pair of indices is duplicative, i.e. it is sensitive to the same properties in sub-hourly variability, the sum of correlation reaches 8.

None of the variability indices is perfectly correlated with any other index. In other words, there is no single variability metric covering all aspects of variability. This formally justifies using a number of variability metrics in the classification.

Overall, four individual indices and two groups of indices can be identified which behave differently in all classes (Table 9). UMC, LMA, and k_{cDNI} are weakly correlated to each other, but not correlated with any other index. Accordingly, these three indices are treated as separate classifiers. Also, the CSFD index has only medium correlation coefficients with other indices and is used as separate classifier.

The other indices show correlations above 6 with at least one other index. Due to their different behavior in classes 4 and 6 they are split into two groups – named the 'low indices' and the 'medium indices' group. This naming is motivated by their location compared to the other indices as in Fig. 9. The group of low indices contains $\Delta k_{cDNI\_\mathrm{mean}}$, $\Delta DNI_{\_\mathrm{mean}}$, UML, and VI. The group of medium indices contains Δk_{cDNI_σ}, $\Delta k_{cDNI\_\mathrm{max}}$, $\Delta DNI_{\_\sigma}$, $\Delta DNI_{\_\mathrm{max}}$, and V.

The index values are far from being constant for each individual class, but compared to the other variability classes, the distributions of values occurring within each variability class differ systematically. The indicator groups (Table 9) are treated separately as classifiers in the automatic classification scheme.

5.2 Automatic classification scheme

Fig. 9 represents Box-Whisker plots for all hourly values occurring for each classifier by variability class.

Class 1 is characterized by maximum LMA and k_{cDNI} reflecting the case of a clear sky day, while all other indices are close to zero. Class 8 is the opposite, with UMC reaching its largest magnitude, but all other indices are around zero. Classes 4 and 6 have highest values in the group of medium indices and also in the group of the low indices. Classes 2 to 7 show large variability of the index values (as indicated by the distance between the 25 and 75 percentiles). Each column in Fig. 9 looks different from all other columns. The box-whisker plots are suitable to clearly discriminate each class if all classifiers are considered.

The index distributions in Fig. 9 are used in the automatic classification scheme as 'reference distributions'. The classifiers median k_{cDNI}, LMA, UMC, and CSFD are treated in a similar way: For each individual hour, the distance between the classifier value in this hour and the median of the reference distribution is calculated. This is repeated for each variability class. The approach is similar for the index-group based classifiers. (the 'low' and 'medium' index group). The distance between the average of all indices in the group from the median of its

Table 7: Variability class characterisation by ramp rates of GHI (after Perez et al., 2011). All median values and the P25 and P75 range (in brackets) are given.

Class	$\Delta GHI_{\_mean}$ [W/m^2]	$\Delta GHI_{\_\sigma}$ [W/m^2]	$\Delta GHI_{\_max}$ [W/m^2]
1	1.17 (0.85, 1.70)	0.8 (0.63, 0.94)	3.0 (3.0, 4.0)
2	7.39 (3.95, 10.92)	9.97 (5.28, 16.54)	45.0 (21.0, 75.0)
3	28.12 (20.44, 38.44)	44.64 (29.68, 64.16)	193.0 (147.0, 266.0)
4	79.63 (70.39, 115.10)	99.73 (72.20, 170.92)	381.0 (236.0, 646.0)
5	19.63 (8.95, 27.19)	17.76 (8.10, 27.42)	82.0 (36.0, 128.0)
6	85.42 (68.46, 105.80)	100.30 (67.02, 117.68)	390.0 (308.0, 465.0)
7	37.51 (21.49, 50.63)	37.14 (22.17, 55.54)	166.0 (95.0, 265.0)
8	5.76 (2.22, 12.12)	4.63 (1.69, 10.05)	20.0 (7.0, 48.0)

Table 8: Variability class characterisation by variability indices of GHI after Stein et al. (2012), Coimbra et al. (2013). All median values and the P25 and P75 range (in brackets) are given.

Class	VI	V
1	1.08 (1.00, 1.21)	0.00 (0.00, 0.00)
2	6.09 (2.77, 8.46)	0.02 (0.01, 0.03)
3	20.36 (13.45, 26.76)	0.10 (0.06, 0.12)
4	51.85 (41.43, 66.55)	0.22 (0.16, 0.25)
5	13.10 (7.38, 16.06)	0.03 (0.02, 0.05)
6	57.71 (39.09, 82.90)	0.18 (0.14, 0.23)
7	23.96 (12.28, 36.90)	0.08 (0.05, 0.10)
8	3.06 (1.33, 8.07)	0.01 (0.01, 0.02)

Table 9: Groups of Indices identified by the correlation analysis.

Classifier name	Group members
mean k_{cDNI}	N/A
Low Indices	Δk_{cDNI_mean}, $\Delta DNI_{\_mean}$, UML, VI
Medium Indices	Δk_{cDNI_σ}, Δk_{cDNI_max}, $\Delta DNI_{\_\sigma}$, $\Delta DNI_{\_max}$, V
CSFD	N/A
LMA	N/A
UMC	N/A

index group is calculated for each individual hour. This procedure is repeated for each variability class. The distances for all classifiers are summed up and the class with the lowest distance sum is the result for that hour. In that way the best fitting variability class with the lowest distance between the median value as given in Fig. 9 and the actual classifier value is chosen.

Since both the quartile range in each class and the spread among the variability classes are small for the 'low indices' group, they are not expected to dominate the classification. But the low index group still improves the automated classification as it includes the k_c indices which are independent of the daily and seasonal cycles.

5.3 Comparing the automatic and visual classification schemes

For validation, the automatic scheme is applied to all hours in the reference database (Fig. 10). Overall, 77 % of all hours are placed into the same class in the automatic and the visual classification. The distributions for all classes peak on or next to the 1:1 line. All classes show a hit rate in the automatic classification above 67 % with 83, 67, 68, 75, 69, 69, 69, 84, and 100 % for classes 1 to 8, respectively. Class 2 has the lowest detection rate with only 24 out of 36 hours classified correctly.

Since the definition of the visual classes is somewhat arbitrary in transition cases between two classes, a second evaluation is made by counting the classification in the visual class or into a neighboring visual class as a success. Borg et al. (2011) report that visual classification accuracy for satellite imagery typically jumps significantly between neighboring classes for different persons (their Fig. 7). Therefore, it is recommended to assess automatic versus visual classification by comparing hit rates including neighboring classes. In our case neighboring classes are classes with consecutive class numbers, but also classes 4 and 6 which are similar in their characteristics (Fig. 5). In that case the detection rate is 90 %. These values are not perfect, but for real data with natural heterogeneity in cloud conditions they are acceptable.

5.4 Example variability classifications in different climate zones and comparison to satellite cloud detection

As an illustration of classification results, the method is applied at four BSRN stations located in Carpentras (CAR, France), Cabauw (CAB, The Netherlands), Sariguren (the station name is CENER/CNR, Spain), and Izana (IZA, Spain). Fig. 11 illustrates the frequency histogram of variability classes for hourly daytime ground observations. Daytime hours must have a minimum solar elevation angle of 5° for the whole hour.

Following Wey and Schroedter-Homscheidt (2014) and as introduced in Section 2, a statistical analysis of cloud occurrence is conducted for the same period of 2012 (Fig. 12). The cloud type is separated into optically thick water clouds in low and medium layers and in water or mixed water/ice phase clouds in a high atmospheric layer. The layer boundaries are defined by 700 and 400 hPa in the US standard atmosphere. Optically thin ice clouds are detected

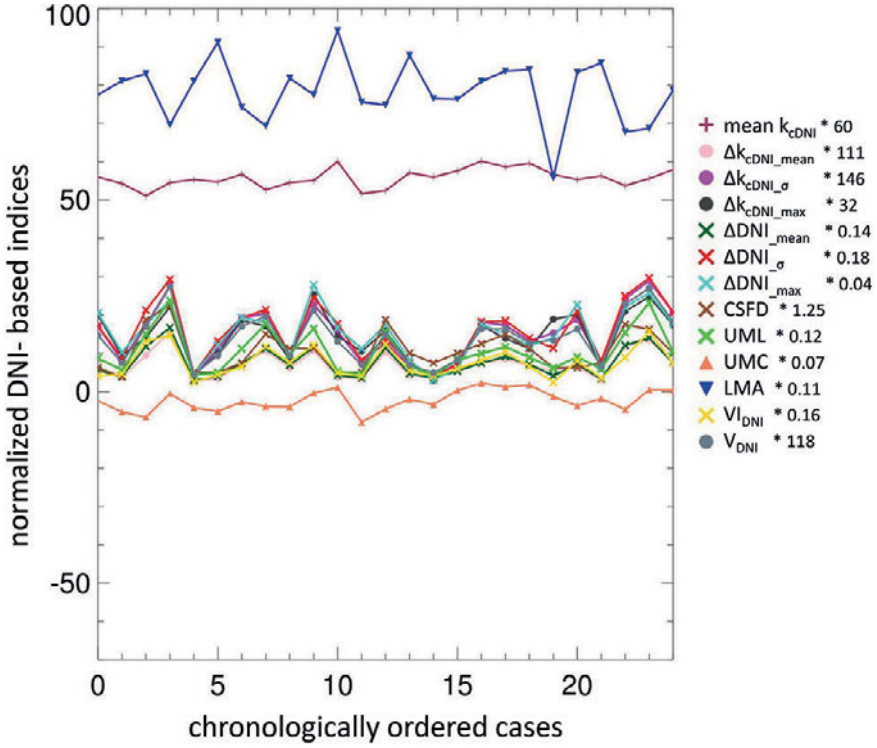

Figure 7: Normalized index values for all hours in class 3 in the reference database in chronological order. The same plot for all classes is given in Annex B.

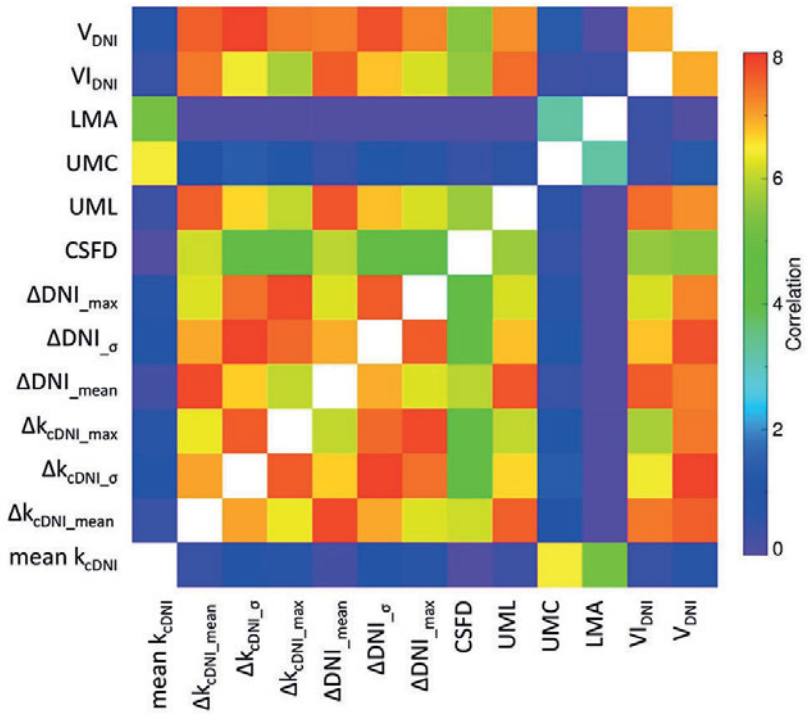

Figure 8: Aggregated correlation heat map for all DNI-based variability indices as sum over all 8 classes. Autocorrelation values on the diagonal are not shown.

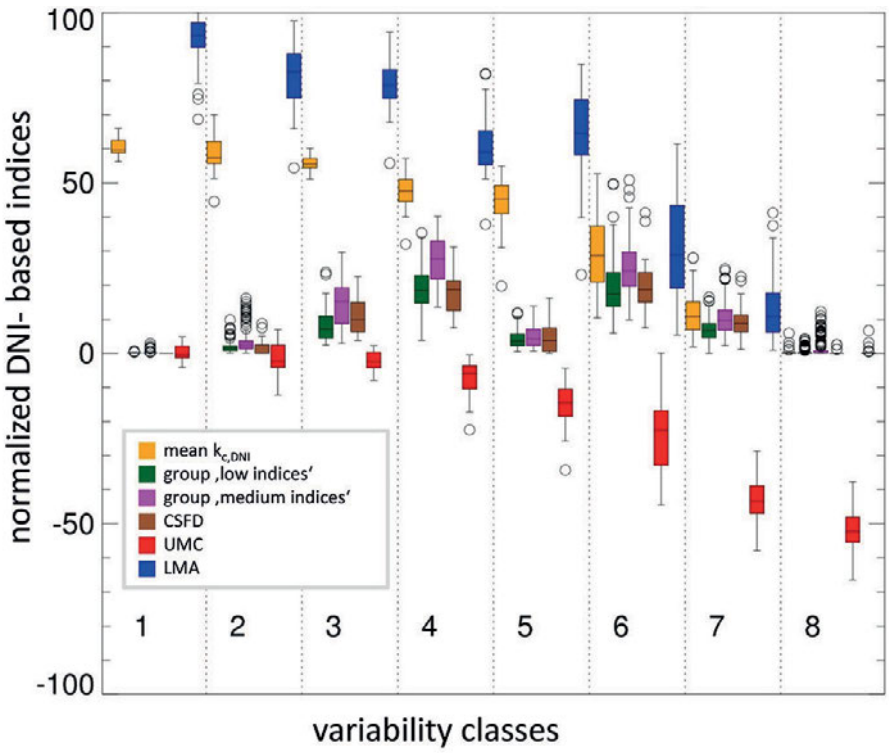

Figure 9: Box-Whisker plots for each DNI-based index group by variability class. Median values are given as black line within each box, the box itself reaches from the lower and upper quartile. The whiskers represent the maximum values in the distribution that are less than 1.5 times the inter quartile distance away from the median. Further outliers are marked as circles.

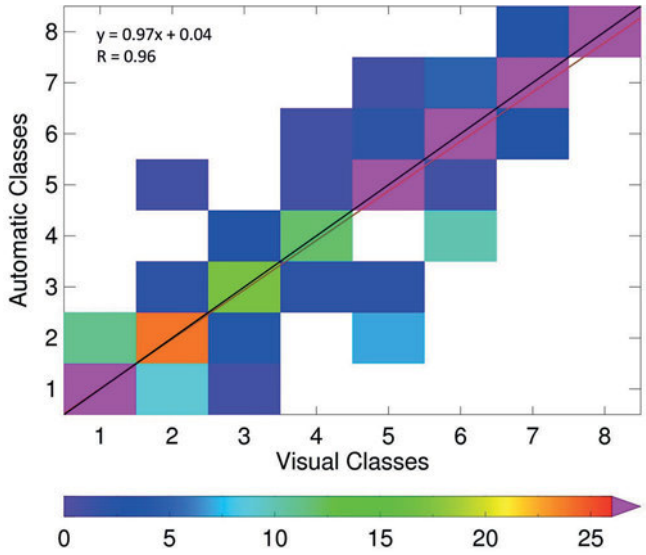

Figure 10: Density scatter plot of the automatic versus the visual classification results for all hours in the reference data base.

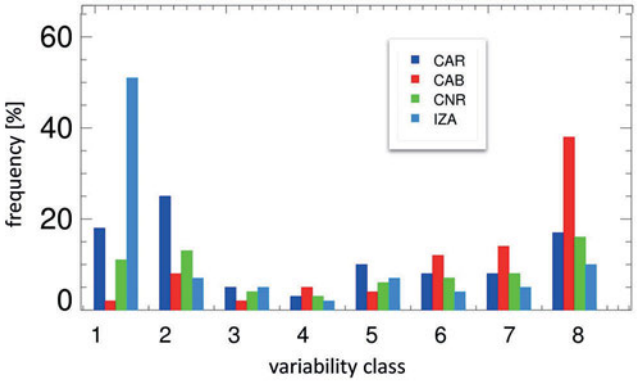

Figure 11: Histogram of classification results for BSRN stations Carpentras, Cabauw, CENER, and Izana based on daytime hours in the year 2012.

as a separate cloud type. Additionally, the scatteredness of clouds is quantified by taking the number of individual contiguous cloud elements in a 29 × 29 satellite pixel sized window around the location of the station into account (for algorithm details see Wey and Schroedter-Homscheidt, 2014).

For Cabauw as a Northern station, variability classes 6, 7, and 8 occur more frequently (Fig. 11), which are the classes with optical thick, scattered, broken or overcast cloud conditions. This is consistent with the majority of optically thick cloud cases found in low and medium layers (Fig. 12). The classes 3 and 5 with high variability but also high DNI are very rare in Cabauw, and near clear sky cases are typically found in class 2 with minor variability. This is also consistent with the large number of optically thin ice cloud cases (Fig. 12), which are often related to class 2 or class 4 patterns.

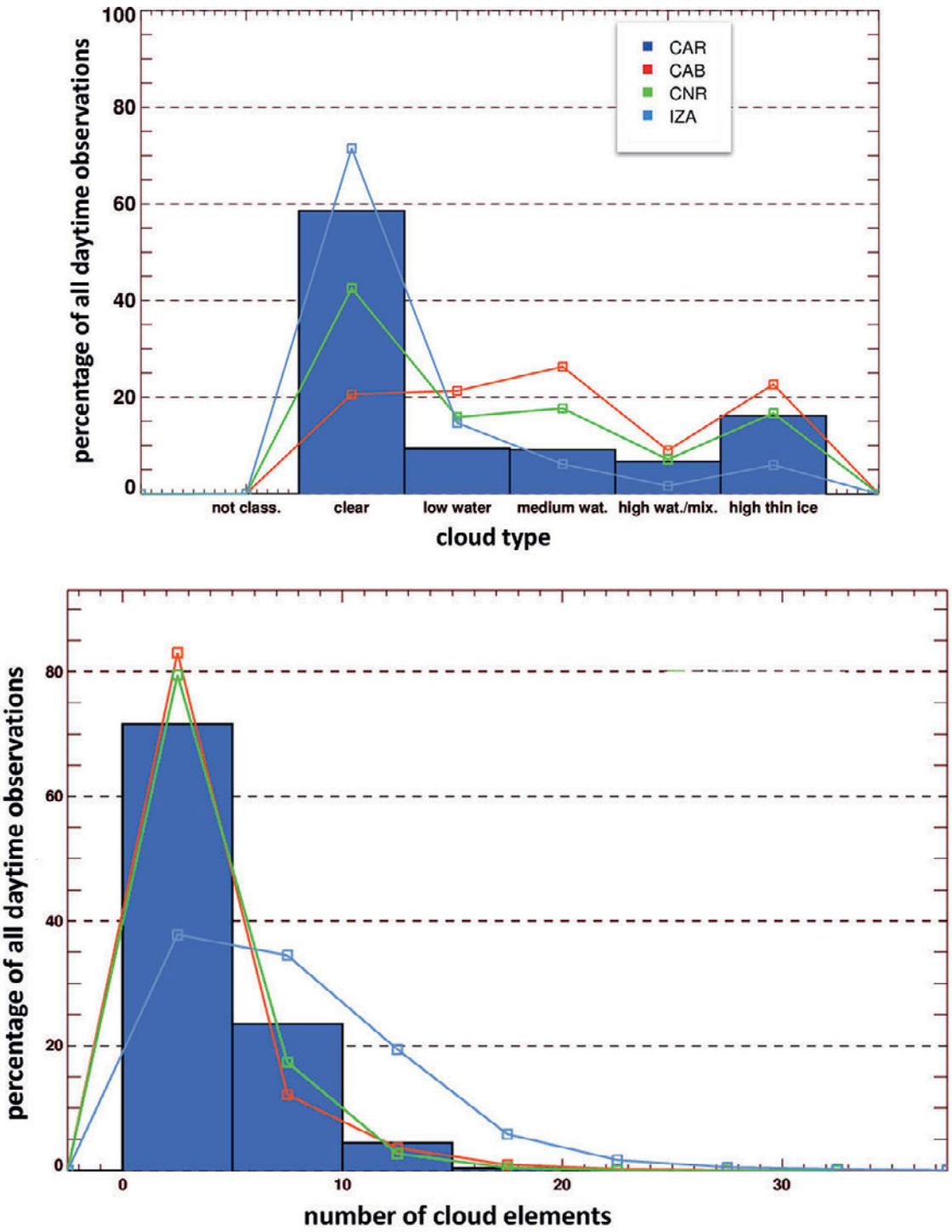

Figure 12: Histogram of cloud types (upper) and number of clouds in a 29 × 29pixel window (lower) as retrieved by MSG/SEVIRI for BSRN stations Carpentras (the reference database), Cabauw, CENER, and Izana based on daytime observations in the year 2012.

CENER shows smaller differences in the frequency of occurrence among the classes with a minimum in the variable, but still high DNI classes 3 and 4. According to the cloud type statistics, CENER has more clear cases than Cabauw, which results in higher occurrences of classes 1 to 3 than Cabauw. Similarly, cloudy conditions are less likely than in Cabauw, resulting especially in less class 7 and 8 cases. The frequency of classes 3 and 4 is inverted – CENER has more class 3 cases with higher average DNI while Cabauw has more class 4 cases. The nearly identical distribution of the number of cloud elements in Cabauw and CENER is surprising at first. The number of contiguous cloud elements in the surroundings can point both to a situation with few small clouds as at CENER but also to a situation with few, but large clouds as at Cabauw. Additional satellite cloud statistics can discriminate between these two cases as discussed in Wey and Schroedter-Homscheidt (2014), but the dif-

ferent DNI variability at CENER and Cabauw discussed in this paper clearly shows that the number of clouds in the neighbourhood alone is not sufficient to distinguish irradiance variability patterns.

Carpentras has a maximum occurrence in classes 1 and 2, but also in the nearly zero DNI class 8. It also has nearly equal medium frequencies in classes 5, 6, and 7, while classes 3 and 4 are less frequent. This agrees with the fact that the most frequent cloud type is optically thin ice clouds, which typically result in the low varability and high DNI class 2, and sometimes classes 3 and 4. Additionally, there is a large number of clear cases which result in the maximum occurrence of class 1.

Izana has a large peak in class 1 in cloud free conditions which is supported by the maximum number of clear cases in the cloud type identification compared to the other locations. Class 8 ranks second and class 5 ranks third. The most frequent cloud type is a low water cloud. The associated meteorological conditions bring a large number of small scale clouds in the surroundings, as reflected in the cloud number statistics in Fig. 12b. Low or medium DNI, but high variability classes 5, 6, and 7 are expected to prevail in these conditions. The number of cloud elements in the surroundings is very high in Izana, but the unique geographical situation as a mountaintop station may mean that often surrounding clouds are below the station elevation and will not affect it. Therefore, the high variability classes 4, 6, and 7 are less frequent than expected if assessing the number of cloud elements only. Due to the special location of the Izana observatory, the relation between the spatial variability of clouds and the temporal variability of the DNI is not evident but also not expected.

Overall, it can be stated that the ground observation based automatic variability class identification is consistent with the satellite-based detection of cloud properties such as the cloud type and the typical spatial scatteredness within the surroundings.

6 Conclusions

Variability of direct normal irradiances in the 1 min range is of interest especially for solar energy applications. This study starts with a review of variability indices published previously mainly for the photovoltaic sector by using global horizontal irradiances. This covers step changes of both clear sky indices and irradiances, overshootings above clear sky irradiances, and envelope-based indices.

Based on a visual classification of 1 min DNI ground observations, a reference database of selected hours with different variability conditions is derived. Eight variability classes are distinguished. The reference distribution is derived for 2012 at BSRN Carpentras, which is affected by a large variety of clouds and DNI variability patterns. It is assumed that these variability classes serve as generic and universal classes also at other locations. This assumption is supported by findings of Woyte et al. (2007) who show that the fluctuations in instantaneous clearness index depend strongly on the mean clearness index and the air mass, but not on the location. Consequently, it is assumed that only the frequency of occurrence of the classes will change from year to year and location to location.

Statistics of previously published variability indices for each class are provided to facilitate the application of our classification results for existing users of the previously published indices. The reference database is made available as a supplement to this paper.

A new automatic detection of these variability classes from ground-based 1 min resolved DNI time series is presented. The reference database serves as training data set. The classification by the automatic detection is consistent with the visual classification of the original reference database. The automatic classification method combines a number of the previously suggested variability metrics and is capable of describing various characteristics of variability of interest for different user groups.

The automatic time series classification approach was tested at three other locations and the results are consistent with satellite-based statistics of cloud type and cloud element counts. The reference database at Carpentras contains many realistic cloud and weather conditions as it is being affected by a wide range of meteorological conditions. Therefore, the classification approach is most likely applicable world-wide. In future work we plan to use this assumption to generate artificial 1 min irradiance time series based on satellite detection of variability classes.

Statistics of the occurrence of variability classes can be used to compare station solar resource characteristics quantitatively (e.g. Schroedter-Homscheidt et al., 2016). The variability classes are also suitable to assess e.g. irradiance forecast accuracy as a function of irradiance variability. Such studies provide new insight for forecast developers and are currently e.g. performed in the DNICast project (http://www.dnicast-project.net/, Saint-Drenan and Dubranna, 2017).

The classification as presented is valid for DNI, but statistical characteristics of the variability classes with respect to GHI and especially GHI overshootings are provided as well. Future work is needed to evaluate their usefulness for classifying GHI variability for the photovoltaic sector.

Work is ongoing to derive the variability classes from satellite-based observations of cloud structures and their spatial patterns. This would allow the classification of the meteorological situation and therefore to derive the variability without the need of classifying 1 minute GHI observations directly. Jung (2015) tested this approach already. This method is currently further investigated and a peer-review publication is in preparation.

Hourly time steps are still widely used in the industry for long-term performance simulations. Variability classes may be useful to derive correction factors for hourly resolved performance models of both photo-

voltaic and concentrating thermal power plants or life time correction factors for storage system cycling as a larger occurrence of highly variable conditions at a location will reduce the system's life time. The automatic characterization of each hour may avoid the need for a system performance simulation at 1 minute resolution which is computationally costly and may not be feasible in all simulation software packages. A potential pathway to integrate sub-hourly variability information is to replace hourly irradiance time series by modified, 'effective hourly GHI or DNI' taking into account the variability effects. This is currently under investigation.

Acknowledgements

The authors would like to thank the personnel from the BSRN station at Cabauw, Carpentras, CENER, and Izana for all BSRN observations and the Copernicus team for deriving APOLLO data. We appreciate the approval by the BSRN Carpentras team to publish a subset of their BSRN observations within the reference database. The study received support from the DNICast project (grant agreement no. 608623) within European Union's Seventh Programme for research, technological development and demonstration. It further received support from the PreFlexMS project (grant agreement no. 654984) within European Union's Horizon 2020 research and innovation programme.

Annex 1: The reference database

Thanks to the approval given by the BSRN Carpentras station manager the whole reference database can be published as supplement to this paper. This facilitates usage of the reference database for describing variability effects in user-driven applications. The reference database is provided as a NetCDF file in the following file structure:

Global attributes:

n_minutes = 60	temporal dimension
n_class1 to n_class8	number of cases in each variability class

Datasets: There are 8 arrays consisting of all DNI and GHI observations being classified as part of the reference database. Dimensions are 60 (minutes) and the number of cases.

The array names are: DNI_class1, DNI_class2, DNI_class3, DNI_class4, DNI_class5, DNI_class6, DNI_class7, DNI_class8 GHI_class1, GHI_class2, GHI_class3, GHI_class4, GHI_class5, GHI_class6, GHI_class7, GHI_class8

Figure A1 shows for each variability class the DNI time series as horizontal axis and case numbers as vertical axis. Figure A2 gives the same visualization for GHI. Figure A3 illustrates the beam clear-sky index for all cases, and finally, Figure A4 provides all clear-sky index values for all cases.

Annex 2: Variability index values for all classes

As complement to Fig. 7, all normalized DNI variablity index values for all classes are given in Figure B1.

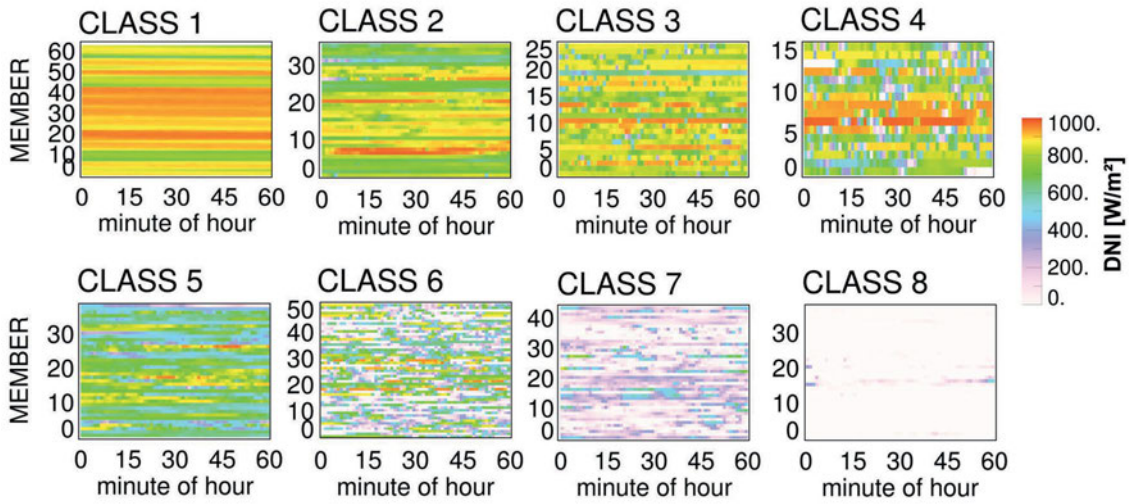

Figure A1: DNI values of all reference database variability class members.

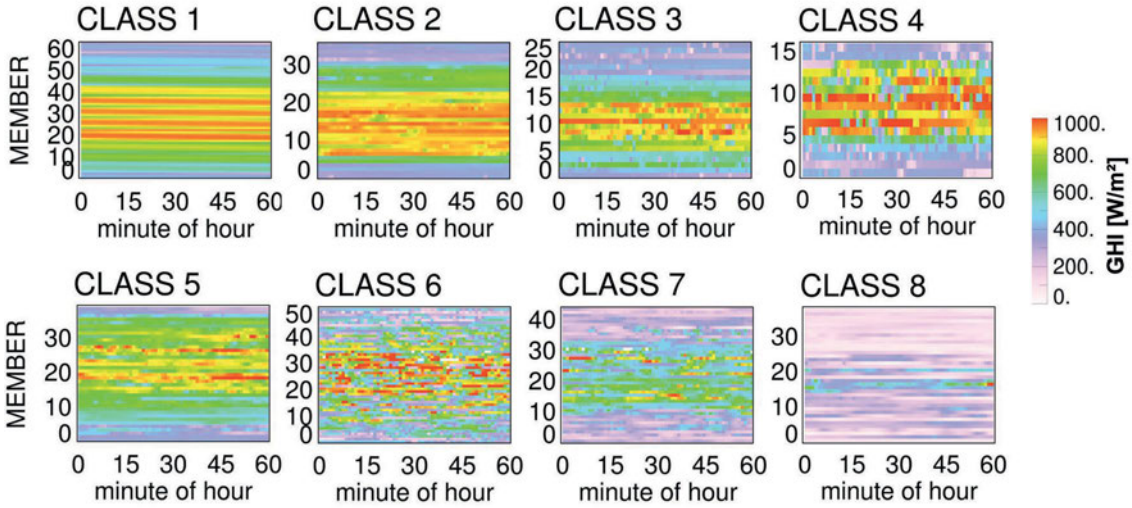

Figure A2: GHI values of all reference database variability class members.

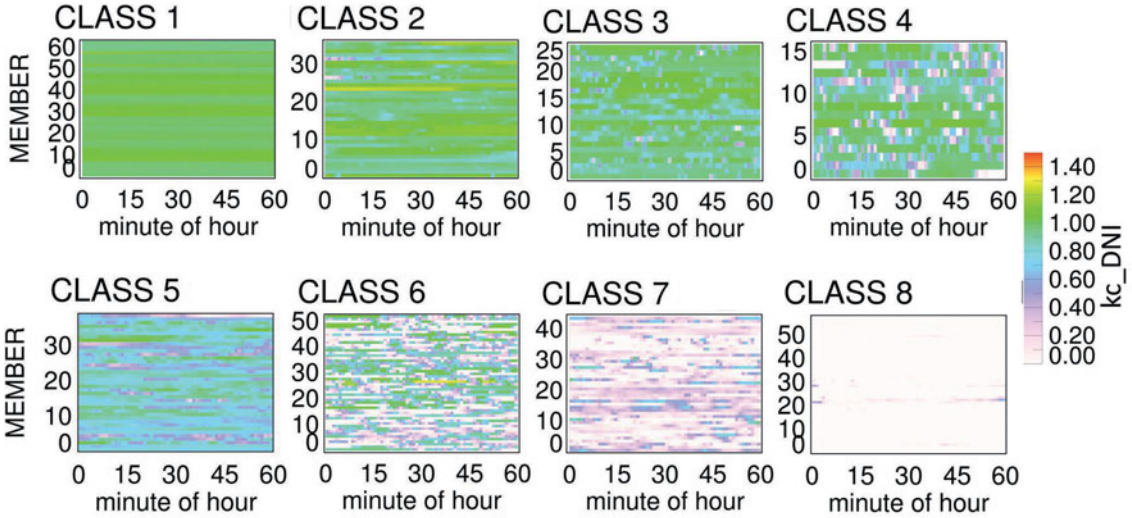

Figure A3: Beam clear-sky index for all reference database variability class members.

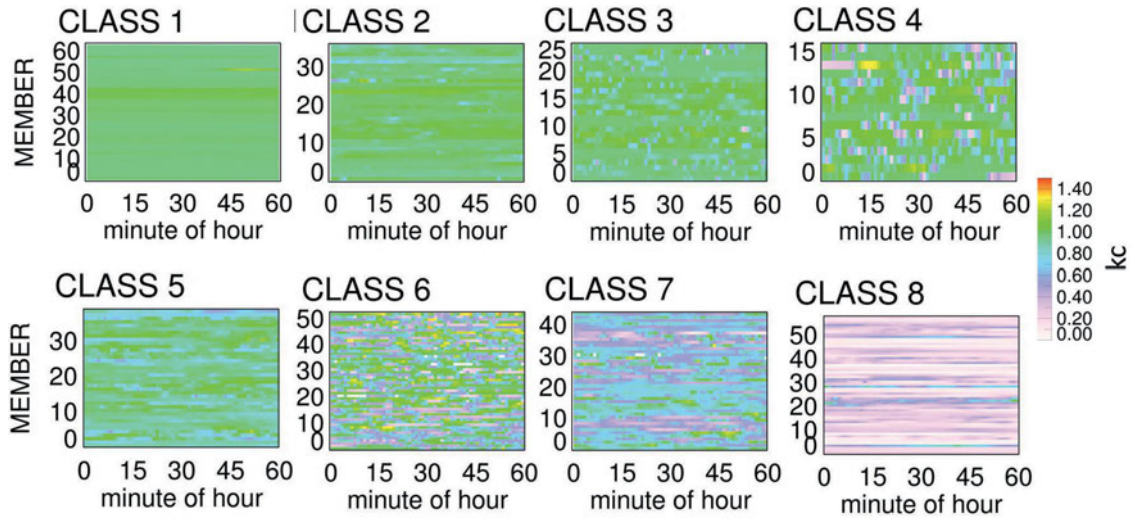

Figure A4: Clear-sky index for all reference database variability class members.

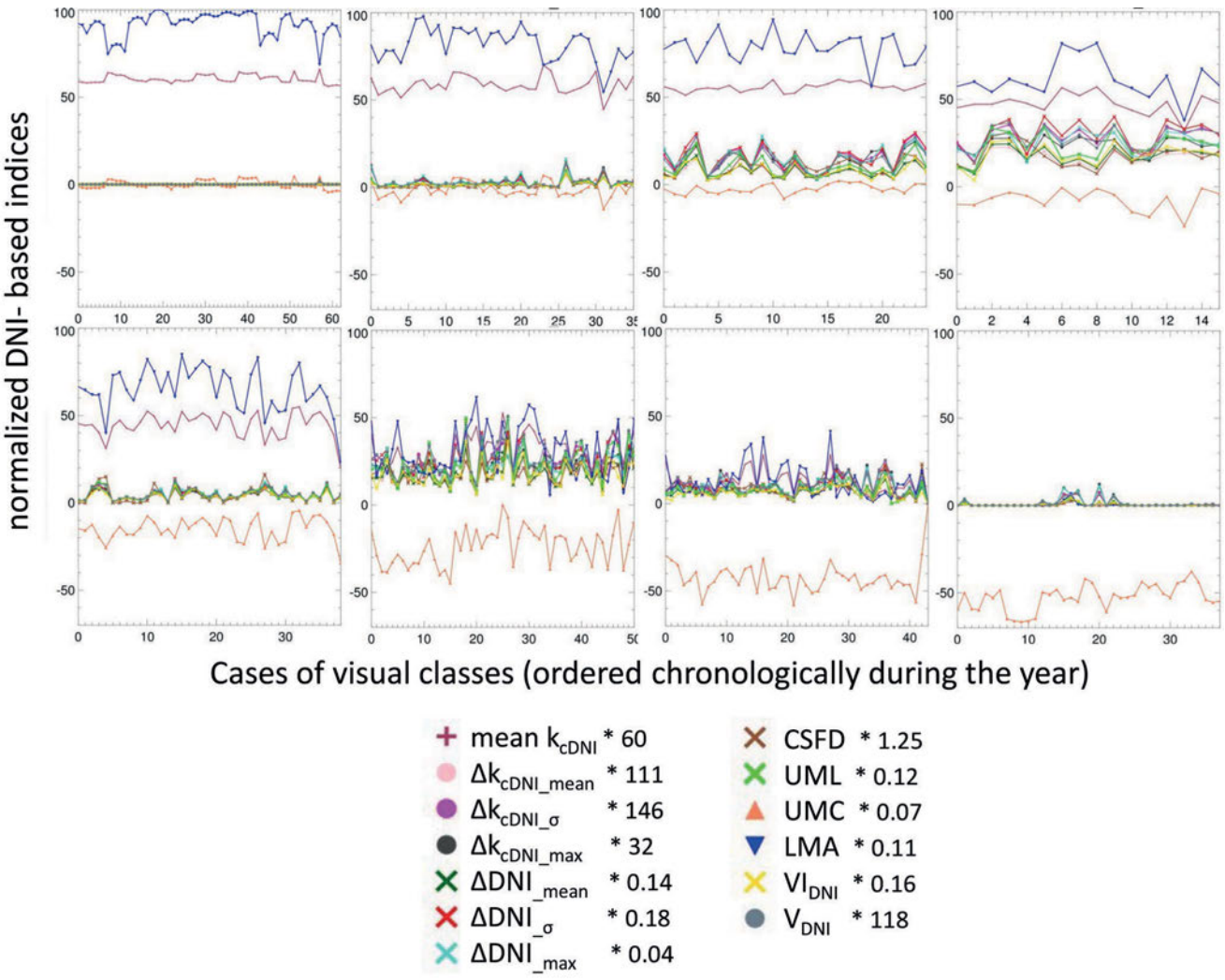

Figure B1: Normalized index values for all hours in all classes 1, 2, 3, 4 (upper row, from left to right) and 5, 6, 7, 8 (lower row, from left to right) in the reference database in chronological order.

References

Anvari, M., G. Lohmann, M. Wächter, P. Milan, E. Lorenz, D. Heinemann, M. Reza Rahimi Tabar, J. Peinke, 2016: Short term fluctuations of wind and solar power systems. – New J. Phys. **18**, 063027, DOI: 10.1088/1357-2630/18/6/063027.

Aukai, T., C. Barker, R. Davis, R., Heilscher, R., Nakafuji, E. Stewart, 2016: Variability of the solar resource and grid operation impacts. – 27th European Photovoltaic Solar Energy Conference and Exhibition, Munich, Germany.

Borg, E., B. Fichtelmann, H. Asche, 2011: Assessment for Remote Sensing Data: Accuracy of Interactive Data Quality Interpretation. – In: Murgante, B. et al. (Eds.): The International conference on Computational Science and its Applications (Iccsa) 2011, Part II, – Lecture Notes in Computer Science (Lncs) 6783, 366–375, Springer.

Coimbra, C.F.M., J. Kleissl, R. Marquez, 2013: Overview of Solar-Forecasting Methods and a Metric for Accuracy Evaluation. – In: Kleissl, J. (Ed.): Solar Energy Forecasting and Resource Assessment. Oxford, 171–194.

Fernández Peruchena, C., M. Blanco, A. Bernardos, 2015: Increasing the temporal resolution of direct normal solar irradiance series in a desert location. – SolarPACES conference, Proceedings in Energy Procedia 69, 1961–1988, DOI: 10.1016/j.egypro.2015.03.199.

Gansler, R.A., S.A. Klein, W.A. Beckman, 1995: Investigation of minute solar radiation data. – Sol. Energy **55**, 1, 21–27, DOI:10.1016/0038-092X(95)00025-M.

Harrouni., S., A. Guessoum, A. Maafi, 2005: Classification of daily solar irradiation by fractional analysis of 10-min-means of solar irradiance. – Theor. Appl. Climatol. **80**, 27–36, DOI: 10.1007/s00704-004-0085-0.

Hirsch, T., N. Martin Chivelet, L. Gonzalez Martinez, M. Biencinto Murga, S. Wilbert, M. Schroedter-Homscheidt, G. Chenlo, J.F. Feldhoff, 2014: Technical report on the functional requirements for the nowcasting method. – Deliverable 2.1 in the Direct Normal Irradiance Nowcasting methods for optimized operation of concentrating solar technologies (DNICast) project, available on http://www.dnicast-project.net/en/index.php.

Hoff, T., R. Perez, 2010: Quantifying PV power output variability. – Sol. Energy **84**, 1782–1793, DOI:10.1016/j.solener.2011.11.005.

Hoff, T.E., R. Perez, 2012: Modeling PV fleet output variability. – Sol. Energy **86**, 2177–2189, DOI:10.1016/j.solener.2011.11.005.

Iqbal, M., 1983: An Introduction to Solar Radiation. – Academic Press, Canada.

Jamaly, M., J.L. Bosch, J. Kleissl, 2013: Aggregate Ramp Rates of Distributed Photovoltaic Systems in San Diego County. – IEEE Transactions on Sustainable Energy 4, 2, 519–526, DOI:10.1109/TSTE.2012.2201966.

Jung, S., 2015: Variabilität der solaren Einstrahlung in 1-Minuten aufgelösten Strahlungszeitserien. – Master thesis, Universität Augsburg, 2015.

Jurado, M., Caridad, J.M., Ruiz, V., 1995: Statistical distribution of the clearness index with radiation data integrated over five minute intervals. – Sol. Energy **55**, 469–473, DOI: 10.1016/0038-092X(95)00067-2.

Kato, T., T. Inoue, Y. Suzuoki, 2011: Estimation of Total Power Output Fluctuation of High Penetration Photovoltaic Power Generation System. – In: Proc. IEEE Power and Energy Society General Meeting, Detroit, USA, DOI: 10.1109/PES.2011.6039560.

Kraas B., M. Schroedter-Homscheidt, R. Madlener, 2013: Economic Merits of a state-of-the-art concentrating Solar Power Forecasting System for Participation in the Spanish Electricity Market. – Sol. Energy **93**, 244–255, DOI: 10.1016/j.solener.2013.04.012.

Koumparou, I., G. Makrides, M. Hadjipanayi, V. Efthymiou, G.E. Georghiou, 2015: Characterization and classification of daily sky conditions in Cyprus and France based on ground measurements of solar irradiance. – 31st European Photovoltaic Solar Energy Conference and Exhibition, Hamburg, Germany.

Lave, M., J. Kleissl, 2010: Solar variability of four sites across the state of Colorado. – Renewable Energy **35**, 12, 2867–2873, DOI:10.1016/j.renene.2010.05.013.

Lave, M., J. Kleissl, E. Arias-Castro, 2012: High-frequency irradiance fluctuations and geographic smoothing. – Sol. Energy **86**, 2190–2199, DOI:10.1016/j.solener.2011.06.031.

Lave, M., J. Kleissl, J.S. Stein, 2013: A Wavelet-Based Variability Model (WVM) for Solar PV Power Plants. – IEEE Transactions on Sustainable Energy **4**, 501–509, DOI: 10.1109/TSTE.2012.2205716.

Lave, M., M.J. Reno, R.J. Broderick, 2015: Characterizing local high-frequency solar variability and its impact to distribution studies. – Solar Energy **118**, 327–337.

Lefévre, M., A. Oumbe, P. Blanc, B. Espinar, B. Gschwind, Z. Qu, L. Wald, M. Schroedter-Homscheidt, C. Hoyer-Klick, A. Arola, B. Benedetti, J.W. Kaiser, J.-J. Morcrette, 2013: McClear: a new model estimating downwelling solar radiation at ground level in clear-sky conditions. – Atmos. Meas. Tech. **6**, 2403–2418, DOI:10.5194/amt-6-2403-2013.

Lohmann, G., A.H. Monahan, D. Heinemann, 2016: Local short-term variability in solar irradiance. – Atmos. Chem. Phys. **16**, 6365–6379, DOI:10.5194/acp-16-6365-2016.

Long, C.N., E.G. Dutton, 2012: BSRN Global Network recommended QC tests, V2.0. – Online available http://www.bsrn.awi.de/fileadmin/user_upload/Home/Publications/BSRN_recommended_QC_tests_V2.pdf.

Lorenz, E., J. Kühnert, D. Heinemann, K.P. Nielsen, J. Remund, S.C. Müller, 2016: Comparison of global horizontal irradiance forecasts based on numerical weather prediction models with different spatio-temporal resolutions. – Prog. Photovolt: Res. Appl., DOI:10.1002/pip.2799.

Ohmura, A., E.G. Dutton, B. Forgan, C. Fröhlich, H. Gilgen, H. Hegner, A. Heimo, G. König-Langlo, B. Mcarthur, G. Müller, R. Philipona, C.H. Pinker, K. Whitlock, K. Dehne, 1998: Baseline Surface Radiation Network (BSRN/WCRP): New Precision Radiometry for Climate Research. – Bull. Amer. Meteor. Soc. **79**, 2115–2136, DOI:10.1175/1520-0477(1998)079<2115:BSRNBW>2.0.CO;2.

Perez, R., R. Aguiar, M. Collares-Pereira, D. Dumortier, V. Estrada-Cajigal, C. Gueymard, P. Ineichen, P. Littlefair, H. Lund, J. Michalsky, J.A. Olseth, D. Renné, M. Rymes, A. Skartveit, F. Vignola, A. Zelenka, 2001: Solar resource assessment: A review. – In: Gordon, J.: Solar energy: the state of the art: ISES position papers. Oxford, 497–576.

Perez, R., S. Kivalov, J. Schlemmer, K. Hemker Jr., T. Hoff, 2011: Parameterization of site-specific short-term irradiance variability. – Sol. Energy **85**, 1343–1353, DOI: 10.1016/j.solener.2011.03.016.

Perez, R., M. David, T.E. Hoff, M. Jamaly, S. Kivalov, J. Kleissl, P. Lauret, M. Perez, 2016: Spatial and temporal variability of solar energy. – Foundations and Trends® in Renewable Energy **1**, 1–44, DOI:10.1561/2700000006.

Perpignan, O., J. Marcos, E. Lorenzo, 2013: Electrical power fluctuations in a network of DC/AC inverters in a large PV plant: Relationship between correlation, dis-

tance and time scale. – Sol. Energy **88**, 227–241, DOI: 10.1016/j.solener.2012.12.004.

Remund, J., C. Calhau, L. Parret, D. Marcel, 2015: Characterization of the spatio-temporal variations and ramp rates of solar radiation and PV. – International Energy Agency, Photovoltaic Power Systems Programme (IEA PVPS), Task 14, Subtask 1.3. IEA PVPS report T14-05:2015, ISBN 978-3-906042-35-0.

Saint-Drenan, Y.M., J. Dubranna, 2017: Validation of nowcasted DNI methods, deliverable D4.3 in DNICast (Direct Normal Irradiance Nowcasting Methods for Optimized Operation of Concentrating Solar Technologies). – Available at http://www.dnicast-project.net/documents/D4.3%20Validation%20of%20nowcasted%20DNI%20methods.pdf.

Schade, N.H., A. Macke, H. Sandmann, C. Stick, 2007: Enhanced solar global irradiance during cloudy sky conditions. – Meteorol. Z. **16**, 295–303, DOI:10.1127/0941-2948/2007/0206.

Schepanski, K., L. Klüser, B. Heinold, I. Tegen, 2015: Spatial and temporal correlation length as a measure for the stationarity of atmospheric dust aerosol distribution. – Atmos. Env. **122**, 10–21, DOI:10.1016/j.atmosenv.2015.09.034.

Schroedter-Homscheidt, M., J.L. Casado Rubio, C.M. Fernández Peruchena, M. Gaston Romero, L. Guierreiro, 2016: Validation sites. – PreFlexMS project report, deliverable D4.2, http://preflexms.eu/

Skartveit, A., J.A. Olseth, 1992: The probability density and autocorrelation of short-term global and beam irradiance. – Sol. Energy 49, 6, 477–487, DOI:10.1016/0038-092X(92)90155-4.

Skartveit A., J.A. Olseth, M.E. Tuft, 1998: An hourly diffuse fraction model with correction for variability and surface albedo. – Sol. Energy **63**, 173–183, DOI: 10.1016/S0038-092X(98)00067-X.

Stein, J.S., M.J. Reno, C. Hansen, 2012: The variability index: a new and novel metric for quantifying irradiance and PV output variability. – In: World Renewable Energy Forum, Denver, CO.

Suehrcke, H., P.G. Mccormick, 1989: Solar radiation utilizability. – Sol. Energy **43**, 339–345, DOI:10.1016/0038-092X(89)90104-7.

Tomson, T., 2010: Fast dynamic processes of solar radiation. – Sol. Energy **84**, 318–323, DOI:10.1016/j.solener.2009.11.013.

Tovar, J., F.J. Olmo, F.J. Batlles, L. Alados-Arboledas, 2001: Dependence of one-minute global irradiance probability density distributions on hourly irradiation. Energy **26**, 659–668, DOI:10.1016/S0360-5442(01)00024-X.

Vijayakumar, G., M. Kummert, S.A. Klein, W.A. Beckmann, 2005: Analysis of short-term solar radiation data. – Sol. Energy **79**, 495–504, DOI:10.1016/j.solener.2004.12.005.

Wey, E., M. Schroedter-Homscheidt, 2014: APOLLO Cloud Product Statistics. – Proc. SolarPACES 2013 conference in Energy Procedia **49**, 2414–2421, DOI:10.1016/j.egypro.2014.03.256.

Wiemken, E., H.G. Beyer, W. Heydenreich, K. Kiefer, 2001: Power characteristics of PV ensembles: experiences from the combined power production of 100 grid connected PV systems distributed over the area of Germany. – Sol. Energy **70**, 513–518, DOI:10.1016/S0038-092X(00)00146-8.

Woyte, A., R. Belmans, J. Nijs, 2007: Fluctuations in instantaneous clearness index: Analysis and statistics. – Sol. Energy **81**, 195–206.

Zehner, M., T. Weigl, M. Hartmann, B. Mayer, T. Betts, R. Gottschalg, H. Lösslein, B. Giesler, G. Becker, O. Mayer, 2011: Europaweite Untersuchung des Irradiance Enhancement Effects und erste Analysen der Bedeutung im PV-System. – 26th PV Symposium, Bad Staffelstein, Germany.

The pdf version (Adobe Java Script must be enabled) of this paper includes an electronic supplement:
Table of content – Electronic Supplementary Material (ESM)

Reference Database of the BSRN station (NetCDF file)